AMSE JOURNALS-AMSE IIETA publication-2017-Series: Modelling B; Vol. 86; N°1; pp 198-220
Submitted Jan. 2017; Revised March 15, 2017, Accepted April 15, 2017
https://doi.org/10.18280/mmc_b.860115

Design of Linear Shaped Charge for Controlled Rock Fragmentation of Brittle Material

*Zhenyang Xu, **Yanning Yu, ***Jun Yang

*College of mining engineering, University of Science and Technology Liaoning, Anshan, China (xuzhenyang10@foxmail.com)
**College of mining engineering, University of Science and Technology Liaoning, Anshan, China (Corresponding author: 1340022796@qq.com)
***State Key Laboratory of Explosion Science and Technology, Beijing Institute of Technology, Beijing, China (yangj@bit.edu.cn)

Abstract

Based on a similar theory, a concrete model experiment and field experiment were designed to solve the problem of non-drilling breakage of large rock in blasting engineering. On this basis, smoothed particle hydrodynamics was utilized to calculate the most ideal bursting height. The results show that stress concentration effects at the ends of the axis are led by linear jet penetration, and the crack area shape is elongated. Furthermore, the expanding direction of the splitting crack is controlled. When the wedge vertex angle is 90°, the fragmentation the specimens is determined. When the wedge vertex angle is 60°, symmetrically radial fracture in center of the specimens is observed. When the wedge vertex angle is 45°, the single splitting surface along the axial direction of penetration on specimens is shown. The intensity of stress concentration of the principal axial plane can be increased by both the decrease of wedge vertex angle and the increase in length of the linear charge. Moreover, the numbers of fragments can be reduced, and the size of fragments can be increased.

Key words

Liner shaped charge, crack propagation, stress, splitting

1. Introduction

In various blasting projects, productivity was greatly affected by secondary breaking. Under the circumstances, a control splitting technology was needed to be utilized to split large rock so that drilling could be avoided and splitting morphology could be controlled. Furthermore, the technology could be safely and efficiently applied to a complex work environment, and the explosive energy utilization ratio could be raised to minimize harm.

In the penetration experiment of the conical charge liner, a radial crack and radial fracture on the surface or inside of the specimens were often caused by direct penetration of the jet [1-5]. However, if the conical charge liner was changed into cuneiform charge liner, the jet would achieve a higher rate of converge at the ends of the penetration axis, and the radial crake or fracture was only shown on the principal plane of the linear jet penetration axis. With this method, the ratio of explosive energy utilization was raised. In addition, the large rock could be directly split by the jet without being completely penetrated, and the blasting rock-flies were reduced.

2. Direction of splitting crack propagation

2.1. Characteristics of dynamic response

With the action of the linear jet penetration, the characteristics of dynamic response, which are different from those in conical jet penetration, were shown on large rocks. With the linear jet penetration, the flat shape in the area of fluid power was changed into a shape similar to an oval, and the oval was referred to as a penetration crack. At the same time, the high stress concentration of circumferential tensile stress was formed at the ends of the axis of the ellipse. When stress concentration intensity was larger than the tensile strength of material of the ends, the inwall of the penetration cavity would quickly crack toward the sides. As a result, crack initiation along the principal plane of the linear jet axis of contraction was accomplished.

2.2 Techniques on controlling checking direction of cracks

When the linear jet was penetrating, a stress gradient field was shaped in the large rock, and the area of strongest tensile stress was concentrated and formed by the penetration axis on the principle plane. Meanwhile, a split crack and the expansion were first shown on the plane of the linear jet penetration axis under stress concentration. After the penetration, the central tendency and intensity would last a certain amount of time so that the checking direction could remain stable later.

With the penetration of the linear jet, tension stresses could be found mainly at the ends of the long axis and short axis of the penetration crack [6]. An equivalent simplified method was practiced in circumferential tensile stress, as shown in Fig. 1.

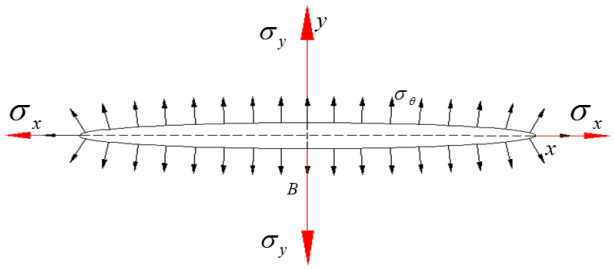

Fig.1. Equivalent tensile stress.

σ_x and σ_y were equivalent loads of circumferential tensile stress loaded on y-axis and x-axis respectively. c was set as the elliptical semi-major axis, and b was the semi-minor axis.

σ_x, σ_y were approximated to be

$$\sigma_x = \int_C^D \sigma dy \approx 2b\sigma_\theta \tag{1}$$

$$\sigma_y = \int_A^B \sigma dx \approx 2c\sigma_\theta \tag{2}$$

As shown in Fig. 2, stress concentrated on A, B, the ends of ellipse major axis, and C, D, the ends of the minor axis.

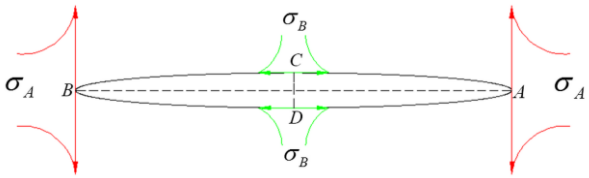

Fig. 2. Tensile stress concentration.

Stress concentration only influenced stress distribution around the crack [7]. Based on elastic theory, the stresses at the ends were as follows:

$$\sigma_A \approx \sigma_y(1+2c/b) \tag{3}$$

$$\sigma_B \approx \sigma_x(1+2b/c) \tag{4}$$

On account of $c>b$, $\sigma_y>\sigma_x$ and $(c/b)>(b/c)$, therefore, $\sigma_A>\sigma_B$. It was known that tensile stresses at the ends of the major axis could still attain the tensile strength even though σ_θ was less than σ_{th}, the fracture critical stress. Relative to the ends of the minor axis, crack initiation expansion happened when the critical fracture stress was immediately reached at the ends of major axis. After the expansion of the main splitting plane, the probability that cracks occurred in another direction was further reduced as jet energy attenuated.

3. Model experiment similarity theory

3.1. Similarity parameters

According to the similarity theory π theorem, in a system with numerous physical quantities, if there were k independent dimensions, the numerous physical quantities could be shown with the function relationship among the similarity criterion of $\pi_1, \pi_2, \cdots, \pi_{n-k}$ [8].This study performed similarity analysis from geosim, material similarity, and similarity in blast dynamics, and made the following assumptions on the similarity of the split system:

(1) Mechanical parameters of the same specimen materials were the same.

(2) Environment temperature was not a concern.

(3) The diffusion of the blast wave and stress wave were at a perfect state.

(4) The impact of size on splitting pattern was left out.

The parameters of analysis of similar selections were as follows:

Main parameters of the liner shaped charge were: the material density the of cuneiform charge liner was ρ_l; the cuneiform charge liner angle was α; the vertex angle of charge shell was α_s; the cuneiform charge liner width at the mouth was W_l; the thickness of the cuneiform charge liner was δ_l; the liner charge length was l_l; charge height was H_c. Main parameters of explosive performance were: the charge density was ρ_c; explosive velocity was D. Main parameters of specimens materials were: density was ρ_r; intensity was σ; wave impedance was $\rho_0 c$; elasticity modulus was E. Main parameters of splitting effect were: penetration depth was p; radius of the jet was r_j.

The impinging jet energy was reflected by the penetration cavity volume, and the cavity volume VP was determined based on penetration depth and the jet's radius. Furthermore, an overall consideration was taken, when the geometric shapes of rock and linear charge structure were similar, the penetration depth P and the jet's radius were regarded as similarity analysis indicators. Additionally, the expansion of the split crack was influenced largely by the geometric shapes of the specimen, so a cylindrical specimen was used in the test, and the geometric dimension was controlled by two parameters: specimen basal diameter *dt* and specimen height *Ht*.

3.2. Similarity criterion

The length dimension *L*, the time dimension *T*, and the strength dimension in the power system were used as fundamental dimensions to indicate the dimensions of the parameters in the experiment, as shown in Table 1.

Similarity analysis was processed from the aspects of geometric similarity, material similarity, and blast dynamics similarity. The dimensional matrix equation set was listed based on the same dimensions, then the equation set was simplified. Finally, when the dimension was 1, every similarity parameter π could meet the similarity theory.

Table 1. Model parameter and dimension.

Name	Symbol	Dimension	Name	Symbol	Dimension
Charge density	ρ_l	$FL^{-4}T^2$	Charge density	ρ_c	$FL^{-4}T^2$
Cuneiform charge liner width of the mouth	W_l	L	Explosive velocity	D	FL^{-1}
Charge thickness	δ_l	L	Specimens density	ρ_r	$FL^{-4}T^2$
Liner charge length	l_l	L	Specimens intensity	σ	FL^{-2}
Charge height	H_c	L	Wave impedance of specimens	$\rho_0 c$	$FL^{-3}T$
Elastic modulus of rock	E	FL^{-2}	Penetration depth	P	L
Radius of the jet	r_j	L			

The second theorem of similarity theory showed that for a charge for some specific shape, penetration depth P and radius of the jet r_j were related to the other 11 parameters.

The parameters in Table 1 could be represented as the following function forms:

$$f(\rho_l, W_l, \delta_l, H_c, \rho_c, D, \rho_r, \sigma, \rho_0 c, E, P, r_j) = 0 \tag{5}$$

α_1, α_2,…,α_{11} were set to indicate the power of ρ_l, W_l, δ_l, H_c, ρ_c, D, ρ_r, σ, $\rho_0 c$, E, P, r_j respectively, so the dimension matrixes were as follows:

Table 2. Dimension matrixes.

--	a_1	a_2	a_3	a_4	a_5	a_6	a_7	a_8	a_9	a_{10}	a_{11}
	ρ_l	W_l	δ_l	l_l	H_c	ρ_c	D	ρ_r	σ	$\rho_0 c$	E
F	1	0	0	0	0	1	0	1	1	1	1
L	-4	1	1	1	1	-4	1	-4	-2	-3	-2
T	2	0	0	0	0	2	-1	2	0	1	0

If W_l, ρ_c *and* D *were basic parameters,* α_2, α_6 *and* α_7 *could be expressed as follows:*

$$\begin{cases} a_2 = -a_3 - a_4 - a_5 \\ a_6 = -a_1 - a_8 - a_9 - a_{10} - a_{11} \\ a_7 = -2a_9 - a_{10} - 2a_{11} \end{cases} \tag{6}$$

In this model experiment, there were eight similarity criterions, α_9, α_3, α_4, α_5, α_8, α_1, α_{10}, and α_{10} had eight variables. They were assigned and calculated respectively according to the sequence of numbers in their subscripts. When the value of one parameter was set to 1, the others were 0.

The results were used to obtain the matrix of π, as shown in Table 3.

Table 3. The matrixes of π.

	a_1	a_3	a_4	a_5	a_8	a_9	a_{10}	a_{11}	a_2	a_6	a_7
	ρ_l	δ_l	l_l	H_c	ρ_r	σ	$\rho_0 c$	E	W_l	ρ_c	D
π_1	1	0	0	0	0	0	0	0	0	-1	0
π_2	0	1	0	0	0	0	0	0	-1	0	0
π_3	0	0	1	0	0	0	0	0	-1	0	0
π_4	0	0	0	1	0	0	0	0	-1	0	0
π_5	0	0	0	0	1	0	0	0	0	-1	0
π_6	0	0	0	0	0	1	0	0	0	-1	-2
π_7	0	0	0	0	0	0	1	0	0	-1	-1
π_8	0	0	0	0	0	0	0	1	0	-1	-2

According to Table 3, similarity criterions could be concluded as follows:

$$\pi_1 = \frac{\rho_l}{\rho_c}, \ \pi_2 = \frac{\delta_l}{W_l}, \ \pi_3 = \frac{l_l}{W_l}, \ \pi_4 = \frac{H_c}{W_l}, \ \pi_5 = \frac{\rho_r}{\rho_c}, \ \pi_6 = \frac{\sigma}{\rho_c D^2}, \ \pi_7 = \frac{\rho_0 c}{\rho_c D}, \ \pi_8 = \frac{E}{\rho_c D^2}$$

On the basis of the analysis, P and r_j could be determined from geometric parameters W_l, δ_l, l_l, W_l and H_c, explosive parameters ρ_c and D, and rock parameters ρ_r, σ, $\rho_0 c$ and E.

In the experiment, π_2, π_3 and π_4 were the main basis for choosing geometric parameters. π_1, π_5, π_6, π_7 and π_8 were the main basis for the choice of material parameters and explosive parameters. Furthermore, in the model experiment, the eight dimensions should be consistent.

3.3. Similarity analysis

For the charge structures with similar geometric shapes, a corresponding similar model was obtained with the conversion of LTSCALE. For a conical charge liner whose diameter was between 40 mm and 178 mm, the similarity was relatively accurate, and the conclusion could be referred to as liner charge experiment. When specimen size was undersized, the boundary effect of the stress wave would be considerably enhanced, so the size should not be too small in case the reliable results were missed.

In conclusion, the size of mode should not be too small.

If concrete was the model material, the ratio of similitude of the model material could be defined as follows:

$$\varpi = \frac{\sigma_m}{\sigma_o}$$

(7)

In Eq. (3.3), σ_m was the intensity of the concrete in the experiment, σ_0 was the intensity of rock in practical engineering.

In different conditions, explosives were different in experiment and in practice, and similitude ratio of the blasting force of explosive was defined as follows:

$$n = \frac{A_m}{A_o}$$

(8)

In Eq. (3.4), A_m was the blasting force value in practice, A_0 was the blasting force value in the experiment.

Affinity constant e in the blasting force was further defined as:

$$e = n\sqrt{\varpi}$$

(9)

Subscript *m* indicated model parameter, and *o* indicated prototype parameter, so:

$$\frac{\rho_{lm}}{\rho_{cm}} = \frac{\rho_{lo}}{\rho_{co}} \Rightarrow \frac{\rho_{lm}}{\rho_{lo}} = \frac{\rho_{cm}}{\rho_{co}} = e$$

(10)

$$\frac{\rho_{rm}}{\rho_{cm}} = \frac{\rho_{ro}}{\rho_{co}} \Rightarrow \frac{\rho_{rm}}{\rho_{ro}} = \frac{\rho_{cm}}{\rho_{co}} = e$$

(11)

$$\frac{\sigma_m}{\rho_{cm}D^2} = \frac{\sigma_o}{\rho_{co}D^2} \Rightarrow \frac{\sigma_m}{\sigma_o} \bullet \frac{\rho_{cm}}{\rho_{co}} = \frac{D_m^2}{D_o^2} = \varpi e$$

(12)

$$\frac{(\rho_o c)_m}{\rho_{cm}D_m} = \frac{(\rho_o c)_o}{\rho_{co}D_o} \Rightarrow \frac{(\rho_o c)_m}{(\rho_o c)_o} = \frac{\rho_{cm}D_m}{\rho_{co}D_o} = \frac{D_m}{D_o} = \sqrt{\varpi e^3}$$

(13)

$$\frac{E_m}{(\rho_c D^2)_m} = \frac{E_o}{(\rho_c D^2)_o} \Rightarrow \frac{E_m}{E_o} = \frac{(\rho_c D^2)_m}{(\rho_c D^2)_o} = \eta$$

(14)

k indicated geometric similarity ratio of the model, so:

$$\frac{\delta_{lm}}{W_{lm}} = \frac{\delta_{lo}}{W_{lo}} \Rightarrow \frac{\delta_{lo}}{\delta_{lm}} = \frac{W_{lo}}{W_{lm}} = k$$

(15)

$$\frac{l_{lm}}{W_{lm}} = \frac{l_{lo}}{W_{lo}} \Rightarrow \frac{l_{lo}}{l_{lm}} = \frac{W_{lo}}{W_{lm}} = k$$

(16)

$$\frac{H_{cm}}{W_{lm}} = \frac{H_{co}}{W_{lo}} \Rightarrow \frac{H_{co}}{H_{cm}} = \frac{W_{lo}}{W_{lm}} = k$$

(17)

From similarity analysis, it could be concluded that different liner shaped charges of different geometrical ratios could be designed directly at varisized concrete specimens.

Splitting effect parameter *P* and r_j should meet the conditions as the following shows:

$$\frac{P_o}{P_m} = k$$

(18)

$$\frac{r_{jo}}{r_{jm}} = k$$

(19)

So the volume of penetration cavity was:

$$\frac{V_{Po}}{V_{Pm}} = k^3$$

(20)

$$C_o / C_m = k \text{ , } \quad b_o / b_m = k \qquad (21)$$

The height-diameter ratio of the concrete specimens was defined as:

$$\tau = H_t / d_t$$

(22)

To control the similarity of concrete specimens, specimen height H_t and its basal diameter d_t should meet affinity laws $H_{to}/H_{tm}=k$ and $r_{to}/t_{tm}=k$ respectively, and for the system which met the affinity laws, its bearing rules could be considered to be similar. As to the charge structure with a similar geometric shape, the corresponding similarity model could be obtained through the conversion of linear scaling factors. The similarity rules of the model and the protomodel were set as follows:

The velocity of the jet head remained unchanged;

The jet's radius and length grew through linear proportionality coefficient;

The jet quality and jet's total kinetic energy grew through linear proportionality coefficient cube;

The penetration depth and the jet's rupture time grew through linear proportionality coefficient;

The penetration cavity volume grew though linear proportionality coefficient cube.

4. Design of model experiment

4.1 Basic configuration of the liner shaped charge

If a shaped charge was installed with a shell, it could prevent detonation form the interference of rarefaction wave. Additionally, angle iron was installed between the bottom of the cover and the shell in case detonation products reveal themselves out of the bottom of cover. A wooden shell of 5 mm thick was used to make the combat area of the linear shaped charge [9].

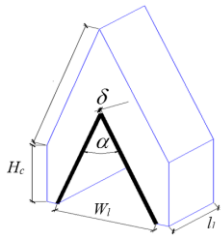

Fig. 3. Schematic of linear shaped charge.

In Fig. 3, α was wedge vertex angle; δ was liner thickness; W_l was cuneiform charge liner width of the mouth; H was charge height; l_l was the length of the linear charge.

4.2 Design of cuneiform charge liner parameters

In order to assure the quality and speed of the jet, thinner copper cuneiform charge liners with the same thickness were used in the experiment [10]. The relationship δ and W_l was:

$$\delta = (0.01\text{-}0.06)\ W_l$$

(23)

W_l should be matched with the specimen size, so:

$$W_l = l_l \approx 0.1 d_t$$

(24)

In Eq. (4.2), d_t was basal diameter of the specimens.

When the vertex angle of cuneiform charge liner decreased, the speed of the jet increased. The largest shape charge angle was 42 o in America [11]. When the vertex angle of the cuneiform charge liner was less than 30 o, the jet stability was erratic. When the vertex angle was between 30～70 o, the speed and quality of the jet were relatively stable. When the vertex angle was more than 70 o, the forming speed of the jet would decrease, the thickness would increase, and penetration depth would dramatically reduce. When the vertex angle was more than 90 o, the cuneiform charge liner would turn over and produce linear projectiles. However, it was possible for the liner shape charge to turn over when the vertex angle of the cuneiform charge liner was less than 90 o. In summary, three kinds of vertex angles of cuneiform charge liner were chosen, which were 45 o, 60 o and 90 o respectively.

4.3 Parameters of explosive

Penetrative performance would significantly increase under a higher detonation pressure [12, 13]. HMX with high detonation velocity was used in the experiment. Its density was 1.902～1.905 g/cm^3, and explosion heat was 5673 KJ/Kg. The numerical simulation demonstrated that when charge density was 1.1 g/cm^3, detonation velocity was about 5100 m/s. Moreover, the detonation velocity was similar to that of the mixed emulsified explosive used in most surface mines, so the experiment would not largely harm the surrounding machines or environment.

4.4 Parameters of charge model

Charge structures with six different kinds of geometric parameters were designed in the experiment, as shown in Table 4.

Table 4. Linear shaped charge parameter table.

NO.	δ	w_l	α	m_l	H_c	l_l	m_c
	/cm	/c	/°	/g	/cm	/cm	/g
1#	0.02	4	90	4.984	4	3	50
2#	0.02	4	90	4.984	3	4	50
3#	0.02	3	60	7.12	4	3	45
4#	0.02	3	60	5.34	3	4	45
5#	0.02	2.5	45	9.256	4	3	42
6#	0.02	2.5	45	6.942	3	4	42

In Table 1, m_l was the weight of the cuneiform charge liner, and m_c was the weight of the charge.

4.5 Parameters of concrete specimens

To avoid error cause by undersized specimens, a column with 30 cm basal diameter and 30 cm height was chosen as the concrete specimens. According to standards of methods of ordinary concrete mechanics performance experiments, the mix proportion of water, cement, sand, and stones was 0.38 to 1 to 1.11 to 2.72, and intensity was 40 MPa, and the specimens should be conserved for 28 days.

5. Selection of bursting height

5.1 SPH Calculation model

Smoothed particle hydrodynamics was a meshless method dealing with free surface, deforming boundary, and great deformation. In the experiment, SPH model of liner shape charge was built under LS-Prepost, and high explosive MAT _ HIGH _ EXPLOSIVE _ BURN was used

in the experiment [14]. Furthermore, JWL was used to express the state of explosive detonation [15], and JOHNSON_ COOK and GRUNEISEN were used in the liner [16].

5.2 Jet free movement patterns

In the experiment, model numbers 1 to 6 were calculated, and instant forms of the jet in 11.96 μS were representatives, as shown in Fig. 4.

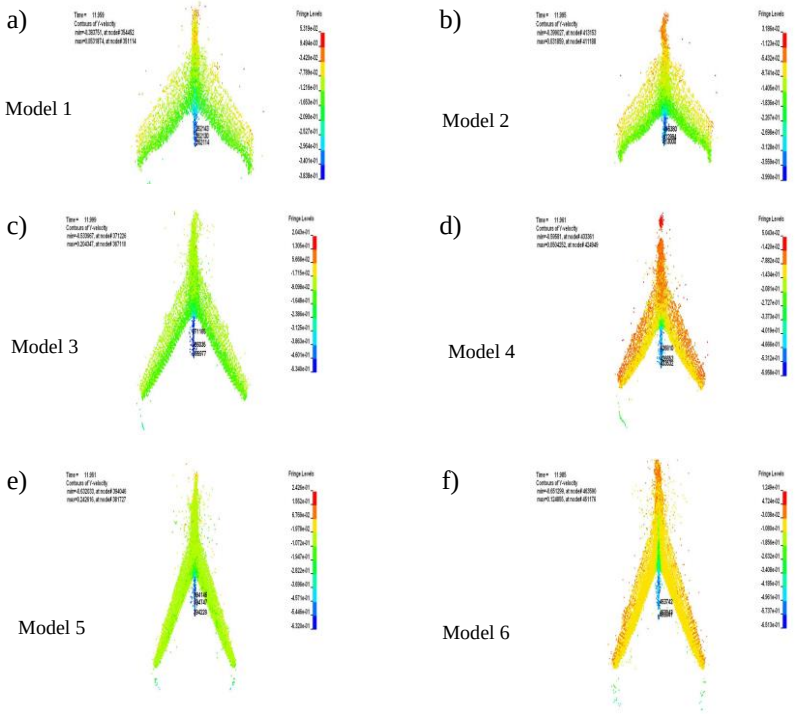

Fig. 4. Jet free movement patterns.

Fig. 5 shows that all six parameters could form a continuous jet, and all the particle morphologies kept uniform as the jet moved. Through the comparison for form processes of the jets, it was found that at 11.985 μS the two specimens with the same wedge vertex angle showed the following similar principles: when the wedge vertex angle was 90 o , the formed jet was relatively short, and the jet tip velocity was lowest; when the wedge vertex angle was 60 o, both jet's patterns and the jet tip velocity were centered; when the wedge vertex angle was 45 o, the jet was the longest, and the jet tip velocity was highest. In the two specimens with the same vertex angles, the jet tip velocity was relatively high when charge height was 4 cm. From this it can be concluded that the charge's height had a far greater impact on jet velocity. Moreover, the number of scattered particles would clearly reduce as the charge's height increased. In fact, the jet had no

effect on penetration after it cracked, but it was the penetration of the jet tip which decided where the crack occurred as well as the direction in which they expanded.

5.3 Kinetic energy of the jet

Kinetic energy of the jet and energy utilization are shown in Fig. 5 and Fig. 6, and kinetic energy of the jet in specimens of numbers 1 to 6 were decreasing. The kinetic energy peaks were 17.1 KJ, 23.2 KJ, 26.7 KJ, 26.8 KJ, 34.8 KJ, 37.2 KJ, and the total kinetic energy of numbers 5 and 6 were obviously greater than the other specimens. The charge in height of numbers 3 and 4 were more than that of numbers 5 and 6, but their combined kinetic energy was lower. Therefore, when the vertex angle of cuneiform charge liner was 60 o, the kinetic energy efficiency would be lower. Explosive payloads in numbers 1 and 2 were least, so their combined kinetic energy was lowest. Furthermore, the increase of kinetic energy was instant, and the kinetic energy of all models reached a peak at 12 μS, and would continuously decrease later.

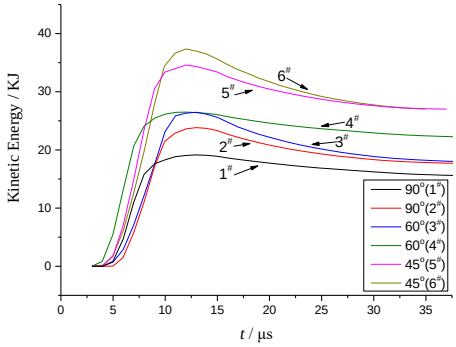

Fig. 5. The total kinetic energy of the jet.

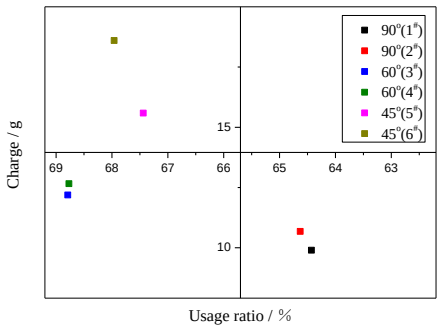

Fig. 6. Utilization of explosion energy.

5.4 The choice of the blasting height

The experiment has determined that the jet first cracked at the jet tip, and as it expanded, the necking and crack expanded rapidly after about 0.14 MS, and the jet completely cracked at 0.29 MS [17, 18]. Furthermore, the penetration performance could be improved through designing a reasonable blasting height. If the blasting height was oversized, the jet would crack before it impacted plate and contrarily, the jet could not stretch to its limitation.

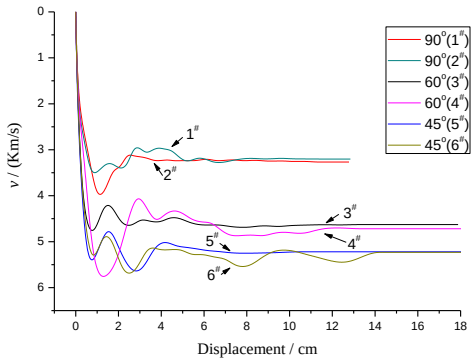

Fig. 7. The jet tip velocity and displacement.

Fig. 7 shows that at the sections where all the jet tip velocity were stable, the total kinetic energy were at two sides of the peak, and the displacement area where the particle of the jet tip was higher than the cuneiform charge liner's mouth could be a favorable blasting height interval [19].

Blasting height interval is shown in Table 5.

Table 5. Shaped charge blasting height.

No.	1#	2#	3#	4#	5#	6#
calculated value/cm	1.8-4.9	2-4.2	1.7-4.3	1.9-4.5	1.8-5	1.7-5
experiment value /cm	4	3	4	3	4	3

6. Analysis of experiment results

6.1 Typical experiment results

The specimen fragment in experiments 1 and 2 were controllable, as shown in Fig. 8 and Fig. 9.

Fig. 8. Fragment effect of experiment 1.

Fig. 9. Fragment effect of experiment 2.

The common results in experiments 3 and 4 were radial fractures on several principal planes, and the radial fractures appeared symmetrically (Fig. 10 & Fig. 11). The radial fracture surface was comparatively flat. Compared with the first experiment, the weight of the cuneiform charge liner in this experiment increased. In addition, when the explosive payload decreased, the splitting effect was more close to the anticipatory form. Hence, it was concluded that different jet forms had a significant impact on the number of the radial fractures on the surface.

Fig. 10. Radial fracture of experiment 3.

Fig. 11. Radial fracture of experiment 4.

6.2 Single splitting surface

Both experiments 5 and 6 showed the effects of a single splitting surface. The degree of crushing on the top of the specimens in experiment 6 was higher than that in experiment 5 because the blasting height in experiment 6 was smaller. The results of experiment 5 are shown in Fig. 12: where the opening displacement on the splitting plane was with an average of 2 cm; the penetration depth was about 5.1 cm; the area of penetration was funnel-shaped; the plane form was an ellipse with a 10 cm around the major axis and 6 cm around the minor axis. The measured data showed that the ratio of the major axis and the minor axis was 1 to 8, but in fact, the dominant factor which affected the expanding direction of the main splitting plane was the shape of the crack shaped by jet tip's penetration

Fig. 12. Splitting effect of experiment 5.

There was obvious dispersion at the end of the jet, and the scale of destruction on the surface of the specimens was enlarged by the dispersing jet, which formed a large pithead and small center. The tops of the specimens show that all the origins of radial cracking on the surface appeared at the penetration hollow's inflection point, which further indicates that the penetration of the jet tip was the determining factor in the expansion of the main splitting plane.

Fig. 13. Splitting crack propagation of experiment

The expanding directions of the splitting crack on the side of the specimens side were divided into three stages (Fig. 13): on it's top, the crack tip's expanding direction changed frequently, but the expanding directions were always on the two sides of the anticipatory main splitting plane; when the crack reached one quarter of the specimens height, the expanding directions were stable, and expanded in a straight line, never deviating from the line; when the crack reached the height of one quarter from the bottom of the specimens, the crack tip clearly curved, which formed a small hole on the left side of the specimens, and then it returned to the original direction and continued to expand.

A small fragment was found at the area near the bottom of the specimens. Moreover, the fragment was only found on one side of the specimens, which was caused by the increase in the uneven level stress field on the bottom of the specimens. In addition, the expanding directions of the splitting crack were also influenced by the original damage and facture, and the splitting crack expanded towards the direction where fracture resistance was lowest caused by the two flaws under cyclic stress, and the expansion was random. The randomness was reduced by the penetration of the liner jet [20, 21]. As has been shown in this experiment, even though the crack tip deviated, it could be returned to the original route under the function of the stress field.

a) b)

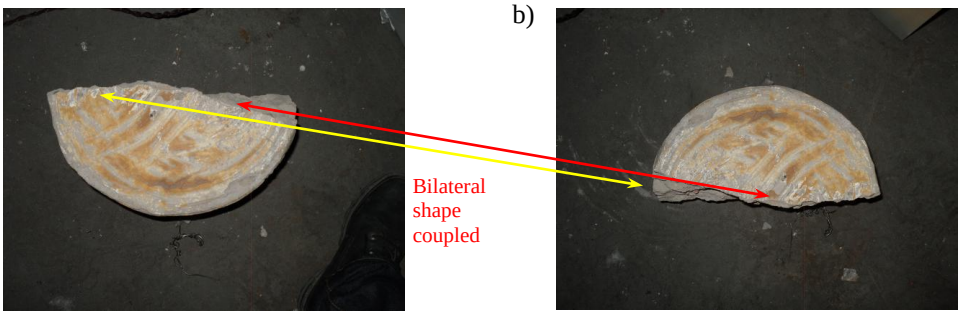

Fig. 14. Bottom splitting effect of experiment 5: a) Left portion; b) Right portion.

The specimen was symmetrically split into two portions, and the bottom of each portion was flat without being broken (Fig. 14). Additionally, the forms of both portions' fracture surfaces were basically coupled, and presented evident brittle fracture characteristics, showing the liner jet's control on the splitting direction and form.

7. Field application

In order to experiment the practicality of the splitting technique, a large rock near the movable crushing station was split directionally on the premise that current production was not disturbed in the mine, and the experiment results of experiment 5 were needed. Four experiments were conducted.

The charge structure was the same with that in model experiment, and emulsion explosive was used. In addition, the detonation velocity was 5100 m/s, the same as that in the model experiment. In Table 6, q was the unit consumption of splitting, which stood for the relation between the charge and rock volume; h was blasting height; H_c was charging height.

Representative data was chosen and is shown in Table 6.

Table 6. Main charge parameters

No.	δ /cm	α /°	H_c /cm	h /cm	m_c /g	q/Kg·m^{-3}
7#	0.3	45	8.2	1	500	0.47

Table 7. Parameters of rock size

No.	L	W	H	V
	/m	/m	/m	/m^3
7#	1.2	1.1	0.8	1.056

It was determined in the 4 experiments that the influence of the large rock's structure should be considered in practice. Experiment 7 with the large rock's layer development was analyzed.

Fig. 15. Placement of the linear shaped charge structure.

Fig. 16. Effect of splitting.

The large rock's layer structure was fully developed, and the interfaces of different layers were easily identified. The liner's linear axis was set on the separating area of the large rock because the area was weak, as shown in Fig. 15. As shown in Fig. 16, the large rock was split evenly, and the broken part only appeared on the top of the large rock.

The farthest scattered distance of the fragments was 1.7 m. Their sizes were between 10 cm and 20 cm. The results showed that the effect direction of the liner jet should be chosen aimed at the structural features of the large rock to increase the jet's energy efficiency.

8. Conclusion

The shape in the region of the crack which produced dynamic response in the large rock was changed by the penetration of the liner jet, and the direction where the splitting crack expanded was controlled by the tension stresses resulting from the penetration gap. Furthermore, the expansion shape of the splitting crack or the radial crack as well as the splitting pattern were determined by the crack region's shape.

In the experiment, the model of the liner shaped charge was verified with SPH as to its reasonability. Metal jets could stretch steadily when they moved, and there were few flying ions. More reliable results would be found as long as the favorable blasting height areas are chosen according to different shapes of liner models based on the jet tip velocity and the total kinetic energy of the jet.

When the wedge vertex angle was 90 °, and the liner shaped charge models were in their optimal blasting height conditions, the specimens could be split. When the wedge vertex angle was 60 °, an even radial fracture was caused on the specimens. When wedge vertex angle was 45 °, the specimens were split into two portions symmetrically along the principal plane of the liner jet's compression axis, and fly fragments were almost zero.

The intensity of stress concentration of the axial principal plane can be increased by both a decrease of the wedge vertex angle and an increase in the linear charge in length. When the wedge vertex angles were the same, the number of fragments can be reduced, and the size of fragments can be increased by lengthening the liner charge.

Acknowledgments

This research was supported by the National Natural Science Foundation of China (Grant No. 51504129), the Anshan Science and Technology plan (Grant No. 3490), and the Liaoning Provincial Department of Education Project (Grant No. L2015263).

References

1. J.A. zukas, High velocity impact dynamics. New York, Wiley-Interscience, 1990.
2. V.P. alekseevskii, Penetration of a rod into a target at high velocity, 1996, Combustion, Explosion and Shock Waves, vol. 2, no. 2, pp. 63-66.
3. J. Sternberg, Material properties determining the resistance of ceramics to high velocity penetration, 1989, Journal of Applied Physics, vol. 65, no. 9, pp. 3417-3424.
4. P. William, W.P. Walters, J.A. Zukas, Fundamentals of shaped charges. John Wiley & Sons, 1989.

5. A.V. Babkin, P.A. Bondarenko, S.V. Fedorov, S.V. Ladov, V.L. Kolpakov, S.G. Andreev, Limits of Increasing the Penetration of Shaped-Charge Jets by Pulsed Thermal Action on Shaped-Charge Liners, 2001, Combustion, Explosion and Shock Waves, vol. 37, no. 6, pp. 727-733.
6. Z.X. Xiao, Z.C. Zhang, X.B. Guo, Research on crack developing law of rock fracture controlled blasting, 2002, Chinese Journal of Rock Mechanics and Engineering, vol. 21, no. 4, pp. 546-549.
7. J.D. Walker, C.E. Anderson, A time-dependent model for long-rod penetration, 1995, International Journal of Impact Engineering, vol. 16, no. 1, pp. 19-48.
8. Q.M. Tan, Dimensional Analysis, Hefei: Press of University of Science and Technology of China, 2005.
9. S. Tanaka, G. Kennedy, K. Hokamoto, Experimental and numerical study on liner shaped charge, 2011, Materials Science Forum, vol. 673, pp. 209-213.
10. Y.C. Li, T. Wu, Q.J. Xu, W.G. Xia, Y. Tang, Numerical Simulation of linear shaped charge jet formation, 2002, Journal of PLA University of Science and Technology, vol. 3, no. 3, pp. 71-75.
11. E. HIRSCH, M. MAYSELESS, Penetration of porous jets, 2010, Journal of Applied Mechanics, vol. 77, no. 5, pp. 1803.
12. S. Lim, Steady state equation of motion of a linear shaped charges liner Meyers, 2012, International Journal of Impact Engineering, vol. 44, pp. 10-16.
13. M.A. Cook, The science of high explosive, New York, Reinhold Publishing Corporation, 1958.
14. H. Couque, R. Boulanger, EFP simulations with Johnson-Cook models, 2007, 23rd International Symposium on ballistics Tarragona, pp. 16-20.
15. G.R. Johnson, W.H. Cook, A constitutive model and data for metals subjected to large strains, high strain rates and high temperatures, 1983, Proceedings of the 7th International Symposium on Ballistics, vol. 21, pp. 541-547.
16. E. Gruneisen, 1912, Theorie des festen zustandes einatomiger elemente, Annalen der Physik, vol. 344, no. 12, pp. 257-306.

17. P.C. Chou, J. Carleone, The stability of shaped charge jets, 2008, Journal of Applied Physics, vol. 48, no. 10, pp. 4187-4195.
18. J. Petit, V. Jeanclaude, C. Fressengeas, Breakup of Copper shaped-charge jets: Experiment, numerical simulations, and analytical modeling, 2005, Journal of applied physics, vol. 98, no. 12, pp. 123-521.
19. Y.N. Shi, C.S. Qin, Instability and break up of stretching metallic jets, 2005, Chinese Journal Of Theoretical and Applied Mechanics, vol. 98, no. 12, pp. 123-521.
20. H.J. Wang, F.L. Huang, Q.M. Zhang, Mechanics effect analysis and parameters study on borehole directional fracture Blasting, 2003, Journal Of China Coal Society, vol. 28, no. 4, pp. 309-402.
21. Z.W. Yue, R.S. Yang, D.M. Guo, H. Cao, J.C. Dong, Dynamic analysis of crack propagation in media containing flaws under the explosive stress wave, 2014, Rock and Soil Mechanics, vol. 35, no. 8, pp. 2048-2414.